





Diffusion in ultra-fine-grained CoCrFeNiMn high entropy alloy processed by equal-channel angular pressing

Yao Jiang^{1,2}, Yuwei Liu¹, Hongbo Zhou², Shabnam Taheriniya², Baixue Bian², Lukasz Rogal³, Jing Tao Wang¹, Sergiy Divinski^{2,*} , and Gerhard Wilde^{2,4,*} 

¹ School of Material Science and Engineering, Nanjing University of Science and Technology, 200 Xiaolingwei Avenue, Nanjing 210094, China

² Institute of Materials Physics, University of Münster, Wilhelm-Klemm-Str. 10, 48149 Münster, Germany

³ Institute of Metallurgy and Materials Science, Polish Academy of Sciences, Krakow, Poland

⁴ Herbert Gleiter Institute of Nanoscience, Nanjing University of Science and Technology, 200 Xiaolingwei Avenue, Nanjing 210094, China

Received: 3 November 2023

Accepted: 5 January 2024

Published online:
21 February 2024

© The Author(s), 2024

ABSTRACT

Grain boundary diffusion in severely plastically deformed (SPD) CoCrFeMnNi high entropy alloy (HEA) has been studied by applying the tracer diffusion technique. After two passes of equal channel angular pressing (ECAP), three ultra-fast diffusion paths in ECAP-processed CoCrFeMnNi HEA were distinguished, which were identified with twin boundaries, high-angle grain boundaries and porosity defects. The enhanced diffusivity is induced by a high strain localization in the vicinity of interfaces in a deformation-induced non-equilibrium state that is correlated with the pronounced deformation twinning due to the low stacking fault energy of the material.

High entropy alloys (HEAs) are nowadays considered as attractive potential engineering materials due to their novel excellent performance, including mechanical properties especially at cryogenic temperatures [1–3], high thermal stability [2, 4] and corrosion resistance [5], to just mention a few.

Zhang et al. [6] indicated that the high mixing entropy of HEAs does not always provide the lowest Gibbs free energy. In particular, complex phases have been found experimentally in HEAs after prolonged

annealing at relatively low temperatures [7–9]. In particular, (severe) plastic deformation was found to stimulate precipitation and decomposition during subsequent annealing treatments [2, 10]. These results suggest that the single-phase HEAs might be in a kinetically stabilized metastable state. Recently, enhanced phase decomposition of nanocrystalline CoCrFeMnNi HEA was reported at 473K after annealing for 1 h [2], although annealing for several years is required to observe similar features on a coarse-grained state of

Handling Editor: Megumi Kawasaki.

Address correspondence to E-mail: divin@uni-muenster.de; gwilde@uni-muenster.de

the same composition [1]. Furthermore, the activation energy of Ni grain boundary (GB) diffusion in HPT processed nanocrystalline HEA was estimated to be 17 kJ/mol larger than that in SPD-processed pure Ni mainly due to the “sluggish” diffusion contribution [11] in compositionally complex alloy systems. At the same time, as expected, it was found to be significantly smaller than the activation energy for the volume diffusion of Ni in the coarse-grained CoCrFeMnNi ($Q_v = 303.9$ kJ/mol) [12], and smaller than the value for Ni diffusion along general high-angle grain boundaries (HAGBs) in that alloy ($Q_{gb} = 221$ kJ/mol) [13] and in pure Ni as well ($Q_{gb} = 121$ kJ/mol [14]). As a reference value for Ni GB diffusion in SPD-processed pure Ni, the authors of [11] have used the reported activation energy of Ni self-diffusion in ECAP-processed Ni with an ultra-fine-grained structure [15].

The estimations by Lee et al. [11] were based on an analysis of nanoindentation creep and the conclusion about the “sluggish diffusion” effect for GB diffusion may be affected by an indirect way of estimating the GB diffusion rates. Note that direct tracer measurements of GB diffusion in annealed coarse-grained HEAs of the CoCrFeMnNi family did not provide any support for the hypothetical “sluggishness” of GB diffusion induced by chemical complexity [13, 16]. Thus, the impact of plastic deformation on GBs and the existence of deformation-modified GBs in SPD-processed HEAs are not unambiguously understood so far. For a recent review on structure, kinetic, and thermodynamic properties of GBs in nano-structured and ultra-fine-grained materials (mainly pure metals and binary alloys) the reader is referred to [17].

Schuh et al. [10] stated that the stimulated precipitation and age hardening effect are mostly connected with a relatively high-volume fraction of HAGBs associated with the microstructure refinement. Nevertheless, a quantitative estimation of the contributions of general HAGBs and SPD-modified HAGBs to the generation of precipitations needs precise measurements of the atomic transport rates in combination with an extended characterization of the microstructure including the inherent defects in the material [18, 19].

Thus, to uncover the specific kinetics of precipitation and thermal stability in HEAs, the present study focuses on the fundamental problem of ‘the influence of severe plastic deformation on grain boundary diffusion.’ The so-called Cantor alloy (i.e., equiatomic quinary CoCrFeMnNi [20]) is selected as a model material, due to its simple single FCC solid solution

phase at elevated temperatures, pronounced thermal stability at low temperatures and excellent plasticity [20–22]. The tracer diffusion technique is applied as a unique strategy to probe the structural states of grain boundaries and their diffusivities at relatively low homologous temperatures [23]. Moreover, as it was mentioned, GB diffusion in the coarse-grained reference alloy was already measured and reliable data are available [13, 16].

The ingots of CoCrFeMnNi for ECAP were prepared by melting Co, Cr, Fe, Mn and Ni metal pieces of at least 99.95% purity using high-frequency electromagnetic induction melting in a water-cooled copper crucible under helium atmosphere. Subsequently, suction casting was performed to shape the ingots into a rod with a diameter of 13 mm. The rods were wrapped in a titanium foil and annealed at 1373 K for 3 days for homogenization followed by water quenching. Afterward, the ingots were cold-rolled alternately in two perpendicular directions to obtain billets of about 12 mm edge length with nearly square cross sections suitable for the ECAP processing. The ECAP processing was conducted at ambient temperature using the B_C route [24] for two passes. At higher pass numbers failure occurred via segmented flow and fracture [25].

The microstructure of all samples was investigated via scanning electron microscopy (SEM) (FEI Nova Nano-SEM 230) implementing electron back-scatter diffraction (EBSD) analysis. The step size was 50 nm and several areas of $50 \times 50 \mu\text{m}^2$ were inspected and merged for a given sample.

Figure 1 presents the measured orientation microscopy image color-coded with respect to the inverse pole figure map for the ECAP-processed HEA sample. A 3-D view is indicated. A hierarchical microstructure is identified, which consists of elongated coarse grains (remnants of the initial grains) with a high density of deformation twins, dislocation walls, low-angle grain boundaries and shear bands. Between some coarse grains, areas of new, nearly equiaxed grains with micron—and submicron sizes are observed.

The misorientation angle distribution in Fig. 1b indicates the fractions of low-angle grain boundaries (LAGBs), $\Sigma 3$ twin boundaries (TBs) and general HAGBs that were approximately 0.63, 0.13 and 0.24, respectively. The significant role of the deformation twinning during room-temperature ECAP processing can be explained by the low stacking fault energy (SFE) of CoCrFeMnNi HEA (of about 20 mJ/m^2 [26]). The coarse initial microstructure (grain size $\sim 250 \mu\text{m}$

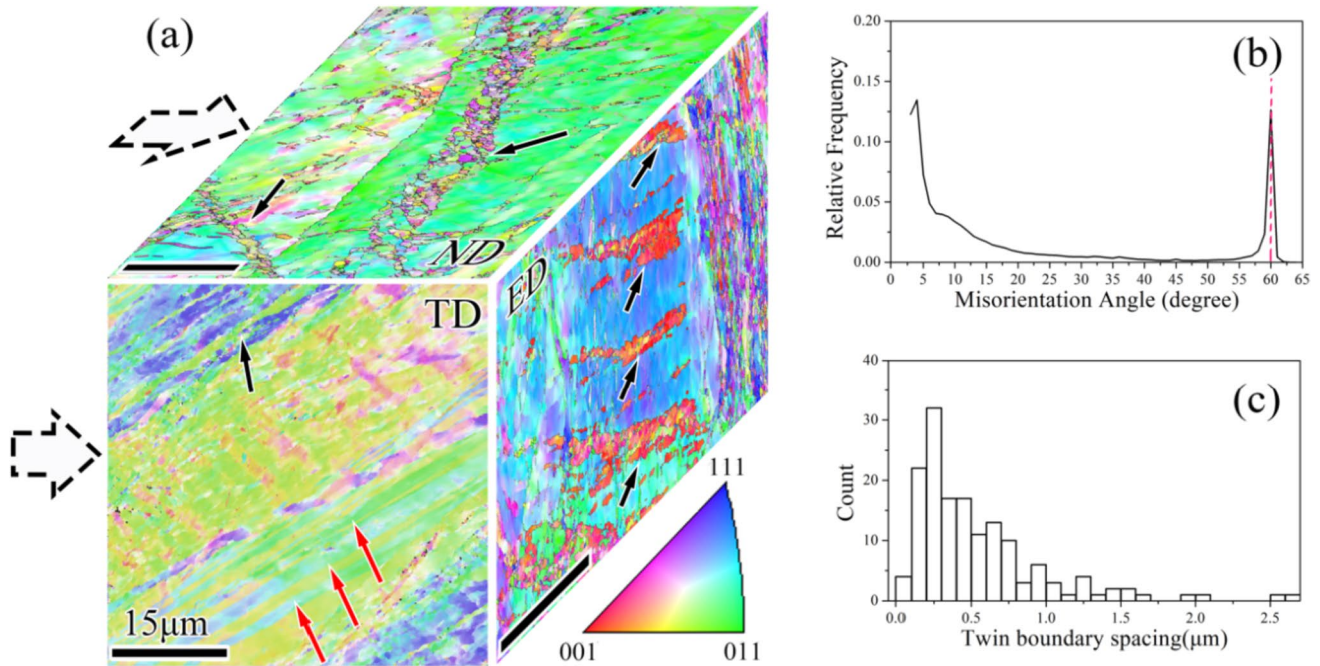


Figure 1 Severely plastically deformed microstructure of the CoCrFeMnNi high entropy alloy obtained after 2 ECAP passes (route B_C) at room temperature. The corresponding misorientation angle and twin boundary spacing distributions are given in (b) and (c), respectively. In (a), the deformation twins and shear bands are indicated by red and black arrows, respectively. The inset color legend indicates out-of-plane crystallographic orienta-

tions of planes parallel to the three main processing directions of ECAP processing (Extrusion direction (ED), Transverse direction (TD) and Normal direction (ND)) using the inverse pole figure mapping. The thick arrows (on the left) indicate the tracer diffusion direction which was parallel to the ECAP flow direction (i.e., the extrusion direction (ED)). The scale bars in different directions correspond to 15 μm .

[12]) was also perceived as enhancing plastic twinning [27]. According to the statistical analysis for TB spacing (Fig. 1c), the average twin lamellae thickness is about 250 nm and the average distance between the twin lamellae is about 5 μm . By inspecting the microstructure, we noted that the profuse deformation twins usually intersect the initial HAGBs, even cross the entire coarse grains (remnants of the initial grains) and transmit into the neighboring grains. This situation is very similar to the microstructure for HPT-processed CoCrFeMnNi HEA after a shear strain of 2.4 [10]. However, TEM results in the literature [28–30] showed that the twin thickness in HEAs could be reduced to 8–20 nm, indicating that the present estimated twin thickness might be overestimated (and correspondingly their fraction underestimated) due to the relatively low resolution and large step size (50nm) of the EBSD analysis.

Furthermore, due to the twins, some initial HAGBs were severely distorted and segmented, exhibiting a “zipper-like” structure and indicating a high density of incorporated defects and residual local stresses/

strains being characteristic of their deformation-induced “non-equilibrium” state. In addition to HAGBs, the observed deformation twins could be classified into two variants, ascribed to the high strain [1, 28] or the billet rotation during the ECAP processing. In this way, some primary TBs also became diffuse as they were intersected by secondary twins. The average density of geometrically necessary dislocations estimated by the Kernel average misorientation (KAM) is about $1.1 \times 10^{15} \text{ m}^{-2}$, very close to the saturation dislocation density ($0.9 \sim 1.5 \times 10^{15} \text{ m}^{-2}$) reported for cold-rolled HEAs [28]. In contrast, owing to the extremely low SFE inhibiting cross-slip due to the operation of deformation twinning, the estimated dislocation density is slightly lower than the value in our previous study on ultrafine-grained (UFG) Ni prepared by ECAP [15] or HPT [31]. From the viewpoint of microstructure refinement, most UFG grains are usually observed within well-developed shear bands and surrounded by LAGBs (as clearly marked by black arrows in Fig. 1a). As an inherent deformation mechanism carrying the high local plasticity, shear bands are

comprehensively facilitated in low SFE metals due to severe shear strain [32]. Thus, the extensive homogeneous areas containing mainly well-defined UFG grains surrounded by HAGBs, which are normally formed in high-SFE materials [33, 34], were seldomly observed here. The overall microstructure characteristics of the ECAP-processed HEA share similarities with low-SFE steel, such as TWIP steels [35, 36] and Cu–Al alloys [32], rather than high-SFE Ni [15, 31] and Al [37] or medium-SFE Cu [38].

As mentioned above, both initial HAGBs and deformation TBs are the dominant internal interfaces in the ECAP-processed HEA sample. Thus, they should provide the dominant contributions to short-circuit diffusion paths for the atomic transport. Note that deformation-induced TBs in SPD-processed Cu were found to feature diffusion rates similar to those of general high-angle GBs [39, 40], i.e., they are significantly enhanced with respect to the diffusion rates of coherent TBs [41]. Formally, this hierarchical microstructure in terms of the short-circuit diffusion behavior resembles that observed in agglomerated nanocrystalline materials [42] or found in other SPD-processed materials [15, 43, 44]. Therefore, an extension of the common classification of GB diffusion regimes by Harrison [45] to encompass the hierarchical microstructure suggested by Divinski et al. [42, 46, 47] is required.

In the present investigation, the conditions corresponding to the formal C-type regime were selected, i.e., the diffusion temperature, T , and time, t , were set in such a way that bulk diffusion can be neglected ($\sqrt{D_V t} \ll \delta$). Here D_V is the bulk diffusion coefficient and δ ($=0.5$ nm [13]) is the GB width. In this pilot study, only the ^{57}Co tracer was used, which was found as most suitable. It has the highest detection efficiency among all accessible gamma tracers for the alloy (^{57}Co ,

^{51}Cr , ^{59}Fe , ^{54}Mn). The value of the Co bulk diffusion coefficient in HEA, D_V , was calculated by extrapolating our previously determined Arrhenius diffusion parameters [48] down to the present diffusion annealing temperature. Formally, the required relation for Le Claire's parameter, α , $\alpha = \frac{s\delta}{2\sqrt{D_V t}} \gg 1$, is safely fulfilled in the present measurements. The value of the corresponding segregation factor s can safely be assumed as about unity. Note that no Co segregation has been recorded in coarse-grained CoCrFeMnNi alloys [13, 16]. Taking the determined Arrhenius parameters of Co GB diffusion in a coarse-grained CoCrFeMnNi alloy [13], one can further confirm the absence of significant diffusion from the surface of the specimen via relaxed high-angle GBs under the present conditions, see Table 1. The typical diffusion lengths $\sqrt{D_{GB} t}$ are less than 10 nm, Table 1. Therefore, the lattice and GB diffusion—as it can be observed in the coarse-grained state along relaxed high-angle GBs—can safely be treated as frozen, and the tracer penetration is governed solely by deformation-induced (or deformation-modified) short-circuit paths.

Thus, the classical Gaussian-type solution of the diffusion equation for one-dimensional diffusion along the x -axis into a semi-infinite body is expected to be valid, if the corresponding diffusion paths can be treated as isolated and acting in parallel. The corresponding penetration profiles plotted as the relative specific layer activity, \bar{C} , vs. the depth squared, x^2 , are shown in Fig. 2.

Having excluded the near-surface points, affected by the remnant tracers and grinding-in effects [44], the deeper branches of the penetration profiles correspond unambiguously to short-circuit diffusion. The effective diffusivity D_{eff} could be determined from the experimentally measured penetration profiles

Table 1 Experimental parameters and the determined coefficients of Co diffusion in ECAP-processed CoCrFeMnNi HEA

T (K)	t (10^3 s)	D_{HAGB}^b (m^2/s)	$\sqrt{D_V t}^a$ (nm)	$\sqrt{D_{\text{GB}} t}^b$ (nm)	$D_{\text{TB}} (\text{m}^2/\text{s})$	$D_{\text{eff,GB}} (\text{m}^2/\text{s})$	$P_{\text{GB}} (\text{m}^3/\text{s})$	$D_{\text{GB}} (\text{m}^2/\text{s})$	α'	β'
673	86.4	2.7E–17	1.2E–02	1.5E+03	4.7E–17	3.5E–15*	1.2E–20	2.4E–14	0.12	64
500	259.2	3.6E–22	1.8E–06	9.6E+00	3.0E–17	9.7E–16*	1.7E–21	3.4E–15	0.09	14
450	259.2	2.8E–24	3.2E–08	8.5E–01		5.9E–17		5.9E–17		
400	259.2	6.6E–27	2.0E–10	4.1E–02		3.0E–17		3.0E–17		
373	2592	1.3E–28	2.3E–11	1.8E–02		4.7E–18		4.7E–18		

^aCalculated by extrapolating the bulk diffusion equation for diffusion of Co in CoCrFeMnNi [16]

^bCalculated by extrapolating the GB diffusion equation of Co in the cast CoCrFeMnNi [48]

*These values are effective and used in the analysis, see text

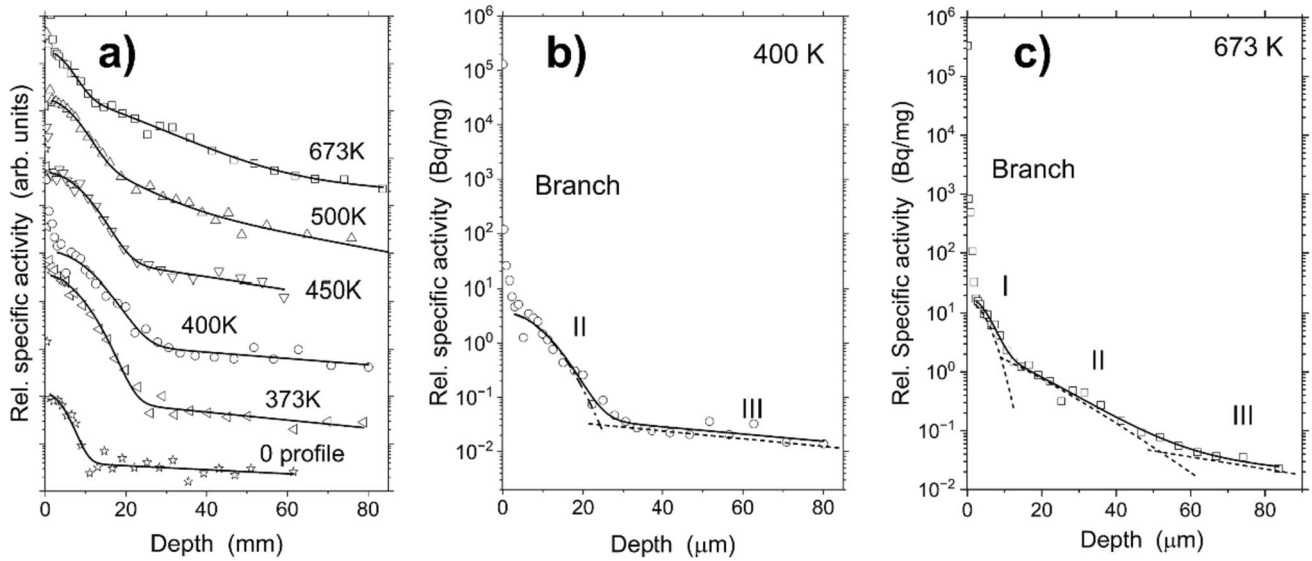


Figure 2 Measured tracer penetration profiles of Co diffusion in ECAP-processed CoCrFeMnNi HEA, in comparison to the zero profile (a). The lines represent the suggested fits, including two or three contributions, see text. The two contributions (Branches

II and III) are recognized below 500 K indicated by the dashed lines for the profile measured at 400 K (b) and three contributions (Branches I, II, and III) are distinguished above 500 K, as an example see the profiles measured at 673 K (c)

by applying the Gaussian solution of the diffusion problem as:

$$D_{\text{eff}} = \frac{1}{4t} \left(-\frac{\partial \ln \bar{C}}{\partial x^2} \right)^{-1} \quad (1)$$

However, as shown in Fig. 2, the measured concentration profiles of Co diffusion in the ECAP-processed HEA do not represent a single short-circuit branch. In fact, one may distinguish usually two (at $T = 500$ K and 673 K even three) diffusion branches. The very first points near to the surface at depths below a few microns are related to the sectioning procedure and they are not included in the present analysis. At the temperatures of 500 K and 673 K, Fig. 2c, two features, *i.e.*, the steep branch (near-surface branch I) and the shallow one (intermediate branch II) correlate with the particular hierarchical microstructure of ECAP-processed HEA (see Fig. 1). We may assume—and a careful analysis will verify this hypothesis—that the two first branches at these temperatures correspond to the contributions of TBs and HAGBs. The long flat tail (deepest branch III) is found to correspond to enhanced atomic transport by micro-cracks and/or percolating porosity [49–51]. This fact is substantiated by the so-called zero-profile, Fig. 2a. It corresponds to

the concentration profile which is recorded without diffusion annealing, just after *deposition* of the liquid tracer solution on the surface of the sample, allowing it to dry, immediately followed by sectioning and decay counting [15]. The deep penetration of the liquid tracer solution is the characteristic feature of percolating porosity often found in SPD-processed Cu or Cu-based alloys [49–51]. Note that the room temperature ECAP-processing of pure Ni does not induce this type of defects which appears only after annealing treatment [19, 23]. It should also be noted that tracer diffusion measurements are highly sensitive to even minute amounts of percolating porosity [44]. A decomposition of the penetration profile as a sum of three contributions, again neglecting the near surface steep branch that is largely influenced by the sample treatment for diffusion measurement, is shown in Fig. 2c.

At temperatures below 500 K, two branches are recognized, Fig. 2b, namely branches II and III (keeping consistent designations at all temperatures). Again, branch III is induced by the micro-cracks or percolating porosity and branch II represents the contribution of grain boundaries. Branch I, most probably being present at these temperatures too, overlaps with the near-surface branch induced by the mechanical sectioning procedure and it cannot be resolved in a reliable way.

The determination of the diffusion characteristics in a hierarchic microstructure with a hierarchy of short-circuit diffusion characteristics is a delicate issue and demands an extensive analysis [42, 52].

As a first approximation, we may use Eq. (1). The corresponding diffusion rates, D_{TB} and D_{eff_GB} , which would characterize the first two branches (if and only if they would correspond to independent short-circuits which provide parallel contributions to the atomic transport) are found to exceed by many orders of magnitude those of the relaxed general HAGBs, see Table 1. Note that branch I is reliably resolved only at two highest temperatures of 500 K and 673 K, Table 1.

This analysis corresponds to the so-called C–C type regime of the interface diffusion in hierarchic microstructures according to Divinski's classification [42, 46, 47] and it is applicable at temperatures below 500 K.

At higher temperatures, when two short-circuit paths are reliably resolved, a further analysis is required. The corresponding characteristic diffusion lengths, $\sqrt{D_{TB}t}$ and $\sqrt{D_{eff_GB}t}$, are important and they have to be smaller as the average distance between the TBs, Λ , and GBs, d_{gb} , respectively. An analysis shows the general high-angle GBs are providing parallel and independent contributions to the diffusion transport, $\sqrt{D_{eff_gb}t} < d_{gb}$, $\sqrt{D_{TB}t} > \Lambda$.

Therefore, a careful analysis suggests that the so-called C-B-type regime holds for the present diffusion conditions in the ECAP processed HEAs, according to Divinski's classification of the diffusion kinetics in hierarchic microstructures [42]. In this type C-B regime, diffusion along TBs proceeds in the Harrison's C-type regime (no out-diffusion into the crystallite bulk), and atomic transport along deformation-modified HAGBs in the B-like regime (with a significant leakage from HAGBs to TBs, which intersect the former).

Thus, the diffusion rates of Co diffusion along SPD-modified HAGBs are characterized by the modified triple products, P_{GB} [42],

$$P_{GB} = \frac{s \cdot \delta \cdot D_{GB}}{\chi} \cong 1.322 \sqrt{\frac{D_{TB}}{t}} \left(-\frac{\partial \ln \bar{C}}{\partial x^{6/5}} \right)^{-5/3} \quad (2)$$

Here s is the solute segregation factor between HAGBs and TBs (it can safely be supposed to be equal to 1 since no strong segregation/desegregation of elements after ECAP processing was observed), δ is the width of the grain boundaries (taken as 0.5 nm [13]),

and D_{GB} and D_{TB} are the coefficients of diffusion along the SPD-modified HAGBs and TBs, respectively. The specific feature of the interaction of the SPD-modified HAGBs and TBs is that out-diffusion does not proceed uniformly but only occurs at the intersections of TBs and HAGBs. Thus, the volume fraction (χ) of the sites where TBs intersect HAGBs is crucial,

$$\chi = \frac{w\delta}{m\Lambda} \quad (3)$$

where $\Lambda = 5 \mu\text{m}$ is the average distance between twin lamellas and w is the number of twin interfaces within a twin lamella. We estimated $w \approx 10$ within the twin lamellas of 250 nm thickness. The factor of $1/m$ represents the fraction of twinned grains where tracer can leak from the HAGBs including a fraction of a particular HEAGB without intersecting twins. Thus, if the multiplicity factor of m is equal to unit, every grain contains equidistant (on average) twins. (This assumption is used in the analysis since we found twin lamellas in all inspected grains.)

The following parameters (in fact, the modified Le Claire's parameters [42]) are crucial for the validity of the C-B diffusion regime and thus of Eq. (2),

$$\alpha' = \frac{s\delta}{2\chi\sqrt{D_{TB}t}}$$

$$\beta' = \frac{s\delta D_{GB}}{2\chi D_{TB}\sqrt{D_{TB}t}} = \frac{P_{GB}}{2D_{TB}\sqrt{D_{TB}t}} \quad (4)$$

The estimations substantiate that $\alpha' \leq 0.2$, and $\beta' \geq 1$ at the two highest temperatures, hence, the conditions of the type C-B regime hold and the present analysis of diffusion in ECAP-processed HEAs is valid. Strictly speaking, the hierarchy of the interfaces is not limited to (deformation-modified) HAGBs and TBs, but includes other types of interfaces, such as LAGBs, dislocation walls and relaxed HAGBs. However, the present experiments were designed to be insensitive to their existence due to the corresponding short diffusion lengths (below and far below 10 nm). The tracer leakage to these interfaces can completely be neglected because the corresponding parameter $\alpha' \gg 1$. The diffusion coefficients of (deformation-modified) TBs and HAGBs determined using Eqs. (1) and (2), respectively, are given in Table 1. Note that the present classification of the diffusion regimes is consistent with the shape of the penetration profiles. In fact, a Gaussian-type contribution for branch II is seen

at lower temperatures, while an almost linear shape (consistent with the $\sim \text{depth}^{1.2}$ functional dependence) is seen at higher temperatures, Fig. 2.

In Fig. 3, the finally determined tracer diffusion coefficients of Co in the ECAP-processed HEA, $D_{TB} = D_{\text{eff_TB}}$ (squares) and $D_{GB} = wP/\Lambda$ (circles), are shown in Arrhenius coordinates and compared with the diffusion rates in several relevant systems. Hereto, the values of D_{GB} are determined using the experimentally measured triple products $P_{GB} = \frac{s \cdot \delta \cdot D_{GB}}{\chi}$.

On one hand, we may compare the measured tracer diffusivities of Co in ECAP-processed CoCrFeMnNi

with the diffusion rates along (relaxed) general HAGBs in well-annealed polycrystalline pure Ni (Ni in Ni [14], Co in Ni [54]), binary FeNi (Ag in FeNi [42]), quaternary CoCrFeNi (Ni tracer [13]) and quinary CoCrFeMnNi [16], alloys. To this end, we have extrapolated the reported values down to the present annealing temperature interval, Fig. 3a. A significant, by orders of magnitude increase of the interface diffusion rates in the ECAP-processed HEA with respect to those in annealed coarse-grained materials is obvious.

On the other hand, in Fig. 3b, the Co diffusion rates are compared with the diffusion rates along the

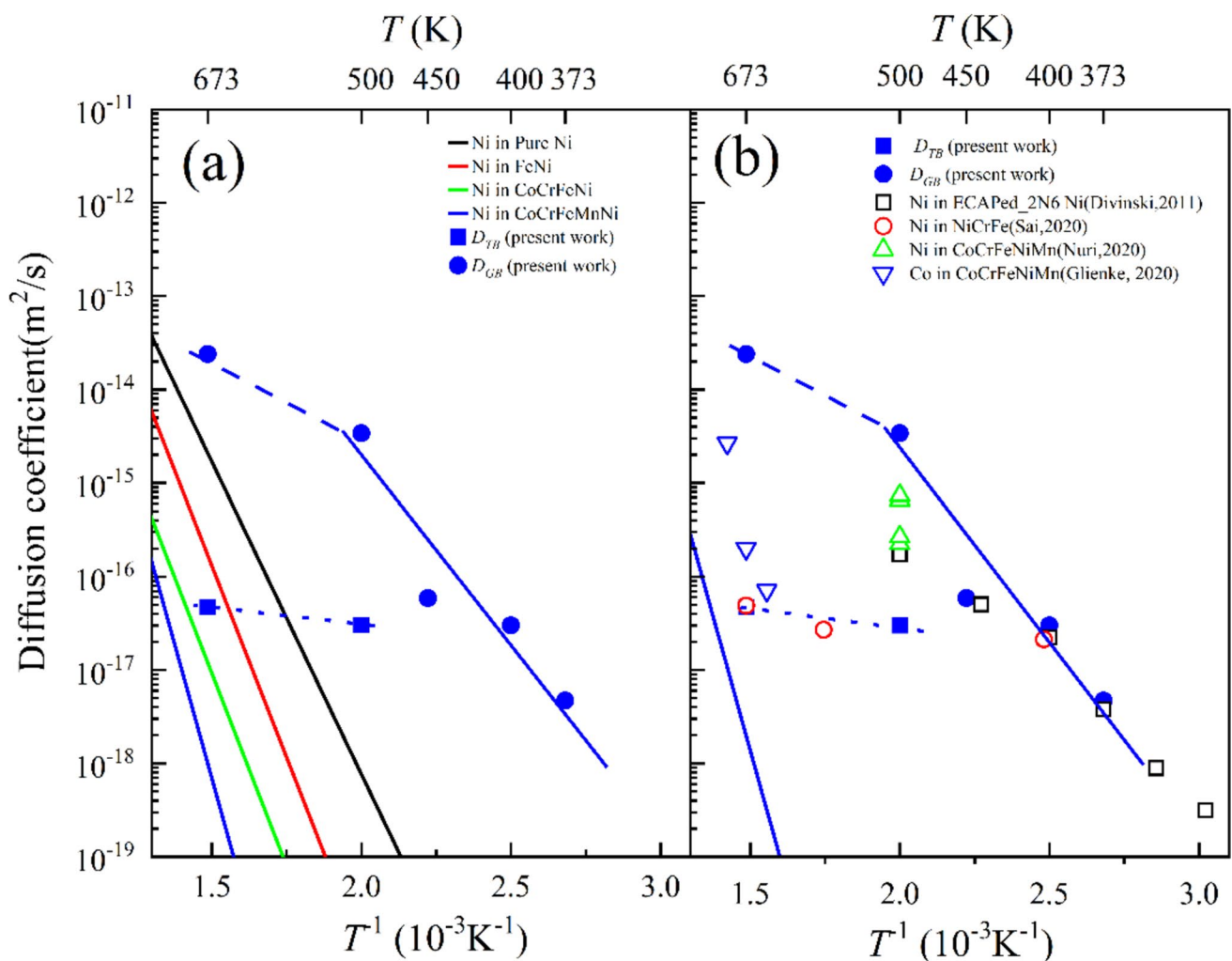


Figure 3 The determined tracer diffusion coefficients of Co in ECAP processed HEA (solid blue symbols) as function of the inverse temperature T^{-1} . In (a), these values are compared with the GB diffusion coefficients of Ni in well-annealed pure Ni (the black lines) [14], Fe-40Ni alloy (the red line) [42], CoCrFeNi (the green line) [13] and the cast CoCrFeNiMn HEA (the solid

blue line) [13]. In (b), a comparison with the GB diffusion rates along non-equilibrium grain boundaries observed in the pressureless sintered nanocrystalline Fe-40wt%Ni alloy [42], the additively manufactured CoCrFeNiMn HEA [53], the long-duration annealed CrNiFe [7], CoCrFeNiMn HEA [16], as well as in the ECAP processed pure Ni [15] is shown.

non-equilibrium grain boundaries observed in the pressure-less sintered nanocrystalline Fe–40wt%Ni alloy [42], the additively manufactured CoCrFeNiMn HEA [53], the long-duration annealed CrNiFe [7], CoCrFeNiMn HEA [16], as well as in ECAP processed pure Ni [15]. The diffusion rates of Ni and Co in these systems can reliably be compared, since the masses, atomic sizes, and electronic structures of Ni and Co are nearly identical [54].

According to the previous investigations, sluggish diffusion in HEAs along HAGBs should be reserved to low temperatures (below 800K) [13]. On the contrary, Fig. 3 substantiates the absence of any hypothetical general diffusion retardation in HEAs after ECAP processing, in this particular case with respect to the SPD-modified GB diffusion transport, as it is seen for Ni diffusion in ECAP processed (B_{C4}) pure Ni [15]. It is obvious that the diffusion rates of Co in the SPD-processed quinary CoCrFeMnNi HEA alloy are similarly fast as Ni in ECAP-processed Ni [15], at the identical annealing temperatures and the same annealing durations.

The Co diffusion rates in ECAP-processed HEA reveal a kink in the Arrhenius plot, Fig. 3. The temperature of the kink, about 500 K, is shifted to a higher temperature relatively to that seen in ECAP-processed pure Ni, Fig. 3b. In Ref. [15] the appearance of the kink has been related to the relaxation of the deformation-modified state of HAGBs. This mechanism holds probably in the present case, too. On the homologous temperature scale, T/T_m , the kink in ECAP HEA is seen at even higher homologous temperature, since the melting point, T_m , of CoCrFeMnNi is lower than that of pure Ni. Thus, a prolonged relaxation of the deformation-modified state in ECAP HEA is obvious.

The fact that the plastically deformed microstructures of the HEA after ECAP processing provide ultra-fast diffusion paths implies that the grain boundary state governing the diffusivity is fundamentally different. It is obvious that the diffusivity in ECAP processed HEA is significantly higher than that observed in coarse-grained HEA [16], and is about equal to that in fine-grained HEA prepared by additively manufacturing [53] (being faster by a factor of 2 to 5). Note that the diffusion enhancement in as-fabricated HEA by additive manufacturing was explained by a “non-equilibrium” state of the general high-angle GBs [53]. All these values exceed significantly the GB diffusion rates in coarse-grained HEA. The enhanced diffusivities in ECAP-processed HEA might be due to the

much higher local strains and excess energy induced by SPD than by decomposition as it was observed by Glienke et al. [16]. It is also meaningful to mention that the enhanced diffusivities along HAGBs and TBs, especially modified by plastic deformation processing, might be the dominant reason for the prominently precipitation, which usually creates brittle secondary phases and therefore leads to stress concentrations and cracks [25, 55].

The present analysis is based on the knowledge of the element diffusion rates in well annealed polycrystalline and single crystalline counterparts. Since the diffusion experiments are performed under the C-type kinetics, we have to interpret the diffusivities as corresponding to specific short-circuit paths. Definitely, dislocations, low-angle GBs, special GBs, twin boundaries and high-angle GBs have to be considered. For annealed polycrystalline materials, the general (random) high-angle GBs represents typically the short-circuit paths with the highest diffusion rates. The diffusivities along dislocations or low-angle GBs are typically significantly lower [56].

In the particular case of the B_{C2} -processed Cantor alloy, the diffusion rates significantly (by orders of magnitude) exceed those of general high-angle GBs (even those which have undergone a phase decomposition) [16]. Thus, these are not (edge) dislocations which provide the observed “fast” diffusion rates. It is well-known that the GB diffusion rates do not depend explicitly on the grain size [56], because basically similar diffusion rates of Ni in Cu were measured for nanocrystalline Cu (30 to 40 nm grain size) [57], ultra-fine-grained Cu (grain size of about 300 nm) [58], polycrystalline Cu (grain size of 60 to 120 microns) [59] and even bicrystalline Cu (two “grains” of the size of about 4 mm) [60]. Therefore, we conclude that the deformation-modified GBs (aka “non-equilibrium” GBs [17]) are responsible for the corresponding contribution. This explanation is based on our experience of measuring diffusion in SPD-processed materials [15, 39, 44].

In order to understand the mechanism of ultra-fast diffusion, the ECAP processed microstructure, especially the interfaces, after annealing at the identical diffusion conditions was investigated by EBSD analysis and the results are presented in Fig. 4. The absence of recrystallization and/or grain boundary migration during the present diffusion annealing measurements is confirmed, i.e., the diffusion multimodality was not induced by either nucleation or grain boundary

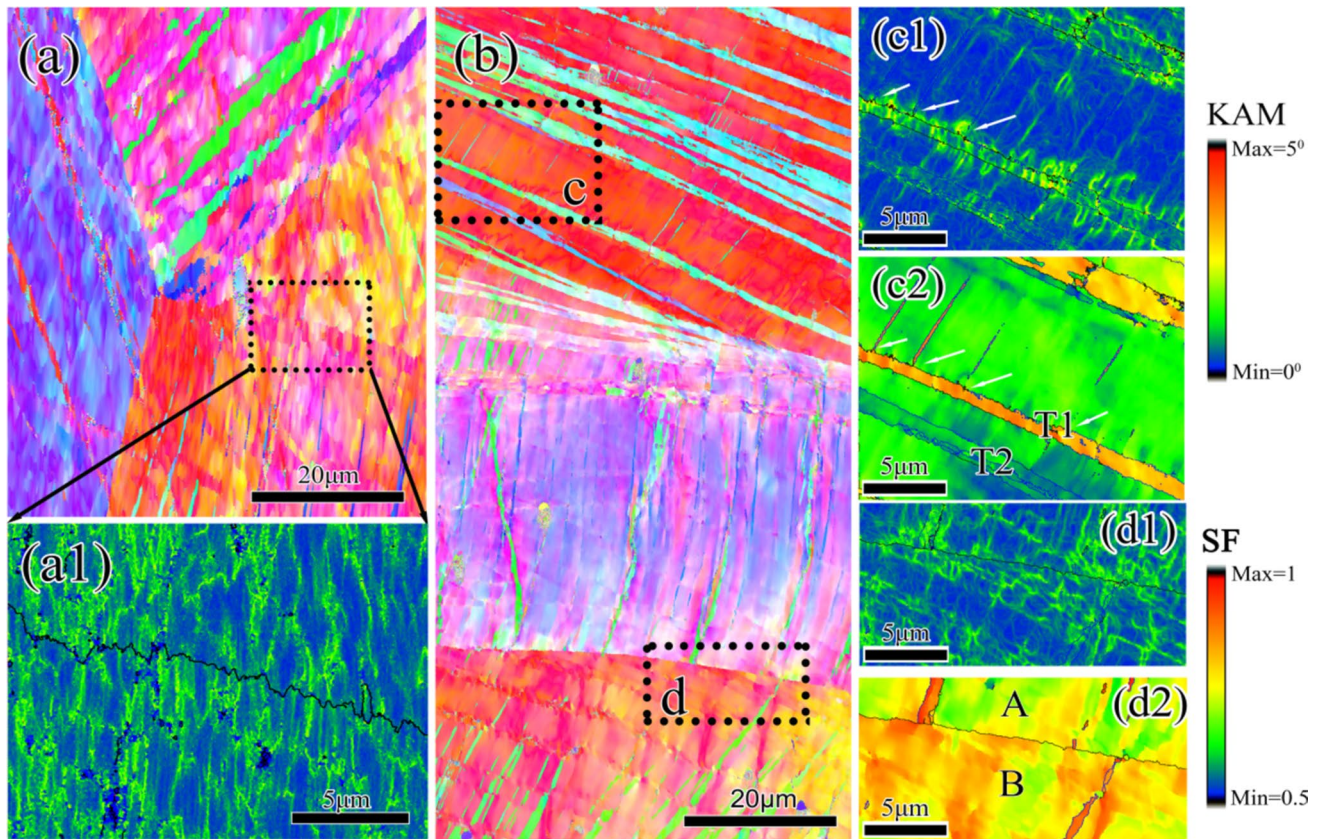


Figure 4 EBSD maps (with color-coding according to the inverse pole figure triangle in Fig. 1) of the ECAP-processed CoCrFeMnNi HEAs after post-deformation annealing for 1 h at 773 K (a), and for 3 days at 500 K (b). In (a1), a magnified image from (a) shows the “zipper-like” HAGBs, presumably in a non-equilibrium state, which is shown as black line. Further mag-

nified images from the framed regions in (b) present the KAM distribution (c1, d1) and the values of the shear factor (SF) (c2, d2), illustrating the strain localization in the vicinity of TBs and HAGBs. The KAM and SF distribution images share the same rainbow legend, respectively.

motion [40]. The ECAP-processed HEA is in a highly non-equilibrium state characterized by a high level of deformation-induced facets and steps at the boundaries even after annealing for 1 h at 773 K, as shown in Fig. 4a, a1. An estimation of the geometrically necessary dislocation density for the present CoCrFeMnNi HEA indicates a slight decrease of the dislocation density, featuring still a very high value of $0.9 \times 10^{15} \text{ m}^{-2}$ after annealing for 3 days at 500 K. Note that a bulk density of dislocations of about $4 \times 10^{15} \text{ m}^{-2}$ is typically reported for ECAP-processed pure Ni [18]. This fact may also evidence the “non-equilibrium” state of the internal interfaces (i.e., deformation-modified HAGBs and TBs) [17, 61].

To shed additional light on the role of severe plastic deformation in the evolution of interfaces of HEAs, the EBSD results obtained on the ECAP-processed CoCrFeMnNi HEA after subsequent annealing for 3 days

at 500 K were selected. The results of the KAM analysis, shown in Fig. 4c1, d1, indicate that strain localizes often in the vicinity of TBs and HAGBs. In the case of TBs, such strain localizations may occur by dislocation glide along the GB planes, i.e., by the conventional GB-mechanism of plastic deformation [62, 63], since the coherent twin boundary is a $\{111\}$ plane which is simultaneously a dislocation glide plane in FCC metals. However, previous studies have claimed that the TBs can transmit dislocations on some slip systems easily, but constitute strong barriers to dislocations motion on others, particularly if the slip is localized on a single system [62]. In this way, premature dislocations that are not transmitted may remain trapped at the TB plane and of course produce pronounced local strains, obviously leading to a higher excess energy. In addition to the strain localization affiliated with the TBs, the dislocation activities at the twin boundaries

will also induce an accumulation of the trapped dislocations in their intersection sites, as shown in the KAM maps (Fig. 4c1, d1). In contrast, Li et al. [64] believed that the secondary twins were generated via partial dislocation emission from the primary TBs to relieve the local strain energy. In any case, the enhanced dislocation density, directly correlated to the local excess energies, will provide relatively high diffusivities for the deformation-modified TBs and HAGBs, similar to those non-equilibrium HAGBs formed in high SFE metals [15, 18, 19, 39, 65]. It is thus safe to expect pronounced strain localization at the intersection sites of TBs and HAGBs.

In contrast to TBs, Fig. 4a1 shows that less strain is localized at the HAGBs. Thus, it might be the reason for the relatively comparable diffusion coefficients of HAGBs and TBs in ECAP processed HEA, presuming that the strain localization might be initiated from the deformation twins. Typically, one would expect by far smaller diffusion rates along relaxed TBs with respect to those along relaxed HAGBs [23]. This view is consistent with the fact that slip along general HAGBs is typically more complicated than along TBs and might involve dislocation climb and annihilation, which are expected to be more difficult than dislocation glide [66]. Regarding grain boundary energy, strain localization formed by impinging dislocations may be accommodated more easily by a general HAGB with more disordered atomic structure and oblique slip planes [67], averting excess energy.

A significance of twinning during plastic deformation of CoCrFeMnNi HEA [30] has been revealed, even for cold rolling [68] and tensile tests [69]. With increasing equivalent strain, there is an increased fraction of twins which gives rise to a more heterogeneous microstructure, especially in low SFE metals [70]. To reveal whether the dislocation activities at TBs have a potential dependency on the orientation of twins, we performed an analysis on their relationship with the maximum Schmid factor under the simple shear stress during ECAP, (named as “shear factor” by Fukuda [71]). The results uncovered that the tendency of dislocation gliding along TBs depends on the variation of the maximum Schmid factor of the TBs and HAGBs, as shown in Fig. 4c2, d2. The comparison with the calculated effective Schmid factor under the applied shear stress showed that it was larger than that at twin lamellae T1 and lower than that at twin lamellae T2. Thus, we expect the parallel slip system to be active at twin lamellae T1 and to be passive at twin

lamellae T2. This is in agreement with the observation that high local strains are visible only at T1 and not at T2. Accordingly, if a TB is oriented with a relatively higher maximum Schmid factor with respect to the simple shear stress vector, dislocation slip and accumulation will have a higher tendency to develop at the TBs.

As it was discussed above, the nonlinear Arrhenius dependence of Co diffusion along deformation-modified TBs and HAGBs is prominent, Fig. 3. It was prescribed to a gradual relaxation of the non-equilibrium states of interfaces with increasing temperature and annealing duration (as in ECAP-processed pure Ni [15]). This also indicates that these excess accumulated dislocations in the vicinity of TBs and HAGBs either are glissile and prone to rearrange and/or annihilate during diffusion annealing to approach a state closer to thermal equilibrium, which manifests as a moderate decrease of the dislocation density from $1.42 \times 10^{15} \text{ m}^{-2}$ in the as-deformed state to $0.9 \times 10^{15} \text{ m}^{-2}$ after aging for 3 days at 500 K or they relax via diffusion-assisted climb of GB dislocations via undisturbed areas of deformation-modified GBs [17, 19].

The delayed relaxation of the non-equilibrium interfaces in deformed HEA with respect to pure Ni, especially on the homologous temperature scale, can be explained by an enhanced thermal stability ascribed to the reduced dislocation annihilation rate during annealing, which may be caused by the requirement of a higher stress for dislocation motion in highly-alloyed HEA materials [30]. In addition, the low SFE and twinning mechanism also contributed to the delayed relaxation by their high degree of dislocation dissociation into partials, obstructing the dislocations annihilation and motions by cross-slip and climb [70].

Investigation of the fatigue behavior of low SFE FCC metals [62, 67] reported that fatigue cracks might initiate at the TBs, despite among all grain boundaries the TB is the one with the lowest energy. With the accumulation of dislocations at the TBs, the initiated micro-cracks from the stress and strain localization might propagate along the shear direction and evolve into fracture failure. Cracks have been confirmed in the highly cold-rolled CoCrFeMnNi HEA after fatigue tests, which cannot be eliminated even after recrystallization annealing at elevated temperature of 1273 K for 2 h [72]. It might be one reason for the fracture of HEA during the third ECAP pass in the present investigation. It is also meaningful to mention that the observed long

flat tails in Fig. 2, which were explained by interconnecting porosity, might be distinguished in contrast to other ECAP processed UFG metals [50, 51]. For the present cast CoCrFeMnNi HEA, the initial grain size reaches several hundred micrometers, far beyond the largest sectioning depth of the present tracer radioactivity measurement. Therefore, the long flat tail might comply with inter-granular crack formation, or otherwise with interconnecting porosity located at the triple junctions [50, 51].

Concerning the feasibility of microstructure refinement for HEAs by severe plastic deformation, the deformability is also influenced by a heterogeneous grain structure and chemical gradients (segregation) in the cast microstructure as a result of the dendritic solidification. In future work, it might be promising to break down the cast dendrites prior to SPD by conventional thermo-mechanical processing, such as hot rolling followed by recrystallization annealing [1, 73], to manufacture crack-free HEA materials. Furthermore, to suppress the strain localization induced by deformation twins, we propose to increase the deformation temperature to increase the stacking fault energy [74]. Another strategy could rely on decreasing the initial grain size to inhibit twinning [75].

Summarizing, the present paper reports the microstructure and kinetic properties of interfaces in ECAP-processed (B_{C2}) CoCrFeMnNi HEA at room temperature. Failure by crack formation occurred during the third pass. The tracer diffusion technique was applied on the ECAP-processed HEA for the first time. Generally, three ultra-fast diffusion paths are distinguished and explained by the formation of inherently hierarchical microstructures, corresponding to deformation-modified twin boundaries, deformation-modified HAGBs, and micro-defects (percolating cracks or porosities). The contribution of deformation-modified twin boundaries becomes clearly visible at higher diffusion temperatures. The high strains in the vicinity of TBs and their intersection sites with the HAGBs (which are remnants of the initial grain boundaries) were identified as the major reasons of the enhanced and particularly high diffusion rates along these interfaces. A non-Arrhenius temperature dependence of the interface diffusivities was observed, confirming that these interfaces are in a deformation-modified (non-equilibrium) state.

Acknowledgements

Y. Jiang would like to thank Chinese Scholarship Council for providing a scholarship to carry out tracer diffusion experiments at University of Münster, Germany. This work was supported by the German Science Foundation under research projects DI 1819/18-1 and WI1899/32-2, by the Natural Science Foundation of Jiangsu Province, China (Grant No. BK20180494), the National Key R&D Program of China (Grant No. 2017YFA0204403), the Natural Science Foundation of China (Grants Nos. 51520105001 and 52301052) and the Fundamental Research Funds for the Central Universities (Grant No. 30923010211).

Funding

Open Access funding enabled and organized by Projekt DEAL.

Data and code availability

Data will be made available upon reasonable request.

Conflicts of interest No conflicts of interest exist for any of the co-authors.

Ethical approval Not applicable.

Open Access This article is licensed under a Creative Commons Attribution 4.0 International License, which permits use, sharing, adaptation, distribution and reproduction in any medium or format, as long as you give appropriate credit to the original author(s) and the source, provide a link to the Creative Commons licence, and indicate if changes were made. The images or other third party material in this article are included in the article's Creative Commons licence, unless indicated otherwise in a credit line to the material. If material is not included in the article's Creative Commons licence and your intended use is not permitted by statutory regulation or exceeds the permitted use, you will need to obtain permission directly from the copyright holder. To view a copy of this licence, visit <http://creativecommons.org/licenses/by/4.0/>.

References

- [1] Otto F, Dlouhý A, Somsen C, Bei H, Eggeler G, George EP (2013) *Acta Mater* 61(15):5743
- [2] Wang J, Wu S, Fu S, Liu S, Yan M, Lai Q, Lan S, Hahn H, Feng T (2020) *Scr Mater* 187:335
- [3] Gludovatz B, Hohenwarter A, Catoor D, Chang EH, George EP, Ritchie RO (2014) *Science* 345(6201):1153
- [4] Otto F, Yang Y, Bei H, George EP (2013) *Acta Mater* 61(7):2628
- [5] Nene SS, Frank M, Liu K, Sinha S, Mishra RS, McWilliams BA, Cho KC (2019) *Scr Mater* 166:168
- [6] Zhang F, Zhang C, Chen SL, Zhu J, Cao WS, Kattner UR (2014) *Calphad* 45:1
- [7] Rajeshwari S, Sankaran KS, Hari Kumar KC, Rösner H, Peterlechner M, Esin VA, Divinski S, Wilde G (2020) *Acta Mater* 195:501
- [8] Laplanche G, Berglund S, Reinhart C, Kostka A, Fox F, George EP (2018) *Acta Mater* 161:338
- [9] Otto F, Dlouhý A, Pradeep KG, Kuběňová M, Raabe D, Eggeler G, George EP (2016) *Acta Mater* 112:40
- [10] Schuh B, Mendez-Martin F, Völker B, George EP, Clemens H, Pippin R, Hohenwarter A (2015) *Acta Mater* 96:258
- [11] Lee D-H, Seok M-Y, Zhao Y, Choi I-C, He J, Lu Z, Suh J-Y, Ramamurty U, Kawasaki M, Langdon TG, Jang J-I (2016) *Acta Mater* 109:314
- [12] Vaidya M, Trubel S, Murty BS, Wilde G, Divinski SV (2016) *J Alloy Compd* 688:994
- [13] Vaidya M, Pradeep KG, Murty BS, Wilde G, Divinski SV (2017) *Sci Rep* 7(1):12293
- [14] Divinski SV, Reglitz G, Wilde G (2010) *Acta Mater* 58(2):386
- [15] Divinski SV, Reglitz G, Rösner H, Estrin Y, Wilde G (2011) *Acta Mater* 59(5):1974
- [16] Glienke M, Vaidya M, Gururaj K, Daum L, Tas B, Rogal L, Pradeep KG, Wilde G, Divinski SV (2020) *Acta Mater* 195:304
- [17] Wilde G, Rösner H, Divinski S (2023) *Mater Trans* 64:1331
- [18] Reglitz G, Oberdorfer B, Fleischmann N, Kotzurek JA, Divinski SV, Sprengel W, Wilde G, Würschum R (2016) *Acta Mater* 103:396
- [19] Divinski SV, Reglitz G, Golovin IS, Peterlechner M, Lapovok R, Estrin Y, Wilde G (2015) *Acta Mater* 82:11
- [20] Cantor B, Chang ITH, Knight P, Vincent AJB (2004) *Mat Sci Eng A* 375–377:213
- [21] Yeh JW, Chen SK, Lin SJ, Gan JY, Chin TS, Shun TT, Tsau CH, Chang SY (2004) *Adv Eng Mater* 6(5):299
- [22] Kottke J, Laurent-Brocq M, Fareed A, Gaertner D, Perrière L, Rogal Ł, Divinski SV, Wilde G (2019) *Scr Mater* 159:94
- [23] Divinski SV (2015) *Diffusion Found* 5:57
- [24] Valiev RZ, Islamgaliev RK, Alexandrov IV (2000) *Prog Mater Sci* 45(2):103
- [25] Semiatin SL, DeLo DP (2000) *Mater Des* 21(4):311
- [26] Zaddach AJ, Niu C, Koch CC, Irving DL (2013) *JOM* 65(12):1780
- [27] Sun SJ, Tian YZ, Lin HR, Yang HJ, Dong XG, Wang YH, Zhang ZF (2018) *Mat Sci Eng A* 712:603
- [28] Stepanov N, Tikhonovsky M, Yurchenko N, Zyabkin D, Klimova M, Zherebtsov S, Efimov A, Salishchev G (2015) *Intermetallics* 59:8
- [29] Gubicza J, Hung PT, Kawasaki M, Han J-K, Zhao Y, Xue Y, Lábár JL (2019) *Mater Charact* 154:304
- [30] Heczal A, Kawasaki M, Lábár JL, Jang J-I, Langdon TG, Gubicza J (2017) *J Alloy Compd* 711:143
- [31] Zhilyaev AP, Kim BK, Nurislamova GV, Baró MD, Szpunar JA, Langdon TG (2002) *Scr Mater* 46(8):575
- [32] An X, Lin Q, Qu S, Yang G, Wu S, Zhang Z-F (2009) *J Mater Res* 24(12):3636
- [33] Jiang Y, Zhu R, Wang JT, You ZS (2016) *J Mater Sci* 51(12):5609. <https://doi.org/10.1007/s10853-016-9862-2>
- [34] Liu F, Yuan H, Yin J, Wang JT (2016) *Mat Sci Eng A* 662:578
- [35] Haase C, Kremer O, Hu W, Ingendahl T, Lapovok R, Molodov DA (2016) *Acta Mater* 107:239
- [36] Timokhina IB, Medvedev A, Lapovok R (2014) *Mat Sci Eng A* 593:163
- [37] Li Z, Zhang PF, Yuan H, Lin K, Liu Y, Yin DL, Wang JT, Langdon TG (2016) *Mat Sci Eng A* 658:367
- [38] Jiang Y, Gu RC, Zhang Y, Wang JT (2018) *Mat Sci Eng A* 721:226
- [39] Wang ZB, Lu K, Wilde G, Divinski SV (2010) *Acta Mater* 58(7):2376
- [40] Wang ZB, Lu K, Wilde G, Divinski SV (2011) *Scr Mater* 64(11):1055
- [41] C. Minkwitz, Chr. Herzig, E. Rabkin, W. Gust, *Acta Materialia* 47 (1999) 1231.
- [42] Divinski SV, Hisker F, Kang YS, Lee JS, Herzig C (2004) *Acta Mater* 52(3):631
- [43] Wilde G, Divinski S (2019) *Mater Trans* 60(7):1302
- [44] Amouyal Y, Divinski SV, Estrin Y, Rabkin E (2007) *Acta Mater* 55(17):5968
- [45] Harrison LG (1961) *Trans Faraday Soc* 57:1191
- [46] S. V. Divinski, F. Hisker, Y.-S. Kang, J.-S. Lee, Chr. Herzig, *Z. Metallkde.*, 93 (2002) 256; *ibid.*, 265.
- [47] S. V. Divinski, Y.-S. Kang, J.-S. Lee, F. Hisker, Chr. Herzig, *Interface Sci*, 11 (2003) 67.
- [48] Gaertner D, Kottke J, Chumlyakov Y, Hergemöller F, Wilde G, Divinski SV (2020) *Scr Mater* 187:57

- [49] Divinski SV, Ribbe J, Baither D, Schmitz G, Reglitz G, Rösner H, Sato K, Estrin Y, Wilde G (2009) *Acta Mater* 57(19):5706
- [50] Ribbe J, Baither D, Schmitz G, Divinski SV (2009) *Phys Rev Lett* 102(16):165501
- [51] Ribbe J, Baither D, Schmitz G, Divinski SV (2009) *Scr Mater* 61(2):129
- [52] Divinski SV, Geise J, Rabkin E, Herzig C (2013) *Ztschrift Fur Metallkunde* 95(10):945
- [53] N. Choi, V. Kulitckii, J. Kottke, B.T. Kavakbasi, J. Choe, J.H. Yu, S. Yang, J.H. Park, J.S. Lee, G. Wilde, S.V. Divinski, *J Alloy Compd* (2020) 155757.
- [54] J. Čermák, 117(2) (1990) 387.
- [55] Zhang Z, Yang Z, Lu S, Harte A, Morana R, Preuss M (2020) *Nat Commun* 11(1):4890
- [56] Paul A, Laurila T, Vuorinen V, Divinski SV (2014) *Thermodynamics, Diffusion and the Kirkendall Effect in Solids*. Springer Int. Publ, Switzerland
- [57] Wegner M, Leuthold J, Peterlechner M, Song X, Divinski SV, Wilde G (2014) *J Appl Phys* 116:093514
- [58] Ribbe J, Schmitz G, Estrin Y, Divinski SV (2009) *Defect Diffusion Forum* 289–292:95–100
- [59] S.V. Divinski, J. Ribbe, G. Schmitz, Chr. Herzig, *Acta Mater.*, 55, 3337–3346 (2007)
- [60] M. Lohmann, PhD Thesis, Münster University, Germany (2004).
- [61] Kolobov YR, Grabovetskaya GP, Ivanov MB, Zhilyaev AP, Valiev RZ (2001) *Scr Mater* 44(6):873
- [62] Stinville JC, Lenthe WC, Miao J, Pollock TM (2016) *Acta Mater* 103:461
- [63] Jin ZH, Gumbsch P, Ma E, Albe K, Lu K, Hahn H, Gleiter H (2006) *Scr Mater* 54(6):1163
- [64] Li N, Wang J, Misra A, Zhang X, Huang JY, Hirth JP (2011) *Acta Mater* 59(15):5989
- [65] Amouyal Y, Divinski SV, Klinger L, Rabkin E (2008) *Acta Mater* 56(19):5500
- [66] M.-J. Caturla, T.G. Nieh, J.S. Stolken, 84(4) (2004) 598.
- [67] Heinz A, Neumann P (1990) *Acta Metal Mater* 38(10):1933
- [68] Otto F, Hanold NL, George EP (2014) *Intermetallics* 54:39
- [69] Laplanche G, Kostka A, Horst OM, Eggeler G, George EP (2016) *Acta Mater* 118:152
- [70] Gubicza J, Chinh NQ, Lábár JL, Hegedűs Z, Langdon TG (2010) *Mat Sci Eng A* 527(3):752
- [71] Fukuda Y, Oh-ishi K, Furukawa M, Horita Z, Langdon TG (2004) *Acta Mater* 52(6):1387
- [72] Tian YZ, Sun SJ, Lin HR, Zhang ZF (2019) *J Mater Sci Technol* 35(3):334
- [73] Liu WH, Wu Y, He JY, Nieh TG, Lu ZP (2013) *Scr Mater* 68(7):526
- [74] Allain S, Chateau JP, Bouaziz O, Migot S, Guelton N (2004) *Mat Sci Eng A* 387–389:158
- [75] A. Kumar Saxena, M. Anupaju, A. Tewari, P. Pant, *Mater Sci Forum* 830–831 (2015) 337.

Publisher's Note Springer Nature remains neutral with regard to jurisdictional claims in published maps and institutional affiliations.